We are IntechOpen, the world's leading publisher of Open Access books
Built by scientists, for scientists

5,500
Open access books available

136,000
International authors and editors

170M
Downloads

Our authors are among the

154
Countries delivered to

TOP 1%
most cited scientists

12.2%
Contributors from top 500 universities

CLARIVATE ANALYTICS
BOOK CITATION INDEX
INDEXED

WEB OF SCIENCE™

Selection of our books indexed in the Book Citation Index
in Web of Science™ Core Collection (BKCI)

Interested in publishing with us?
Contact book.department@intechopen.com

Numbers displayed above are based on latest data collected.
For more information visit www.intechopen.com

Chapter

The Physical Chemistry of Steel Deoxidation and Nozzle Clogging in Continuous Casting

María-Guadalupe González Solórzano,
Rodolfo Morales-Dávila, Jafeth Rodríguez Ávila,
Carlos Rodrigo Muñiz-Valdés and Alfonso Nájera Bastida

Abstract

Nozzle clogging in continuous casting of steel originates by the adherence of alumina particles and other oxides, precipitated during the liquid steel deoxidation, on the refractory material's surface. Hence, these particles' nucleation and growth rates in supersaturated melts are analyzed considering, specifically, the role of the interfacial tensions between alumina, silica, and other oxides and the liquid metal. Weak steel deoxidizers like silicon do not need high supersaturations favoring high nucleation rates, giving particles' narrow size distributions thanks to fast diffusion and Ostwald-ripening coagulation. Strong deoxidizers, like aluminum, need high supersaturation levels leading to broad size distributions. Besides, the morphology of these particles depends on the nucleation and growth mechanisms. The adhesion forces among the deoxidation particles, forming clusters, depending on the morphology and the oxide's chemistry. The stability of the nozzle's clog, adhered to the nozzle's wall, depends on the interface tensions between the melt and the nozzle's refractory surface and between the melt and the inclusion. The results obtained here help set up basic recommendations in steel refining and materials specifications of casting nozzles.

Keywords: steel deoxidation, nozzle clogging, melt supersaturation, nucleation, growth, interfacial tension

1. Introduction

Clogging of mold nozzles, also called submerged entry nozzles (SEN), disrupts the steel casting process, affecting the caster's productivity. The nozzle clogging produces inconsistent flow and temperature variations, steel level fluctuations in the mold, impairment of steel quality, and the steel casting's abrupt interruption. Clogging starts when solid compounds, mainly steel skull and non-metallic inclusions, are non-uniformly deposited at the inner nozzle wall, at some typical preferential zones characterized for neighboring dead flow conditions [1–5]. These inclusions have as primary sources: (1) The reaction between the dissolved oxygen with the deoxidizers [6–9]; (2) re-oxidation in the tundish or the nozzle [10, 11]; and (3) the entrainment of slag or refractory particles [11–14]. Researchers who have worked on the determination of inclusions sources and clogging recognize that

the deposited inclusions at the nozzle wall are mainly alumina inclusions [7–9, 15, 16]. Steel re-oxidation occurs due to possible air aspiration under the flow control valves (slide gate) to maintain the entry flow to the molds [17–19]. Besides, regardless of the refractory nozzle composition (alumina-graphite, zirconia, and magnesia), the steel melt infiltrates the refractory and removes the protective surface [11, 20], allowing the entrapment of refractory particles and inclusion attachment at the nozzle wall.

The non-metallic inclusions come from the steelmaking process; several researchers have focused on studying the variables that induce the inclusion deposition at the inner nozzle wall producing the clogging phenomena [1, 11–14, 16, 21–22]. Steel chemistry and, in particular, steel grades containing titanium, like Ti-SULC, (Ti Stabilized Ultra-Low Carbon Steels), steels enhance the nozzle clogging due to the surface tension properties of this element in liquid steel [23–25]. The wetting of inclusions, rich in Ti oxide, assists in the clustering and compaction of particles. When the ratio Ti/Al is above a threshold, dictated by thermodynamics, the wettability of complex oxides of Ti and Al works intensifying the nozzle's clogging under the presence of oxygen. This series of papers provides an insight into the clogging phenomena while casting these steel grades.

In the present chapter, the authors deal with the physical–chemical aspects of the nozzle-clogging problem by inclusions originated through the deoxidation reactions of steel. Hence, to understand the fundamentals of the problem first, these particle's nucleation and growth are considered using non-equilibrium thermodynamics principles. Second, the influence of the steel refining processes on the deoxidation particle morphology and the relation with their further growth through aggregation and clustering mechanisms is under scrutiny. The analysis continues with studying the thermodynamics related to the oxide particle's adherence to the refractory. Finally, a dynamic analysis lets the establishment of balance among drag, buoyancy, adherence, and lift forces leading to a detachment criterion for an inclusion forming part of a first layer of the clogging. After this work, conclusions and recommendations are provided.

2. Non-equilibrium thermodynamics

2.1 Nucleation and growth rates of oxide inclusions

The nucleation of a foreign phase in an originally homogeneous solution, in the present case an oxide particle in a liquid solution of iron, is driven by the free energy of the reaction.

$$x[M] + y[O] = M_xO_y \tag{1}$$

$$\Delta G_m = \Delta G_m^0 + RTln\frac{a_{M_xO_y}}{h_M^x h_O^y} = \Delta G_m^0 + RTlnQ \tag{2}$$

where Q is the activity quotient, in the thermodynamic equilibrium $\Delta G_m = 0$ and the Eq. (2) changes to,

$$\Delta G_m^0 = -RTlnK_E \tag{3}$$

where K_E is the equilibrium constant, which depends only on the temperature. Combining Eqs. (2) and (3), dividing the result between the molar volume of the oxide results in,

$$\Delta G_V = RTln$$

$$\frac{Q}{K_E} = -RTln\frac{S_0}{V_0} \tag{4}$$

and S_0 is the supersaturation ratio given by,

$$S_0 = \frac{Q}{K_E} = \frac{K_{MO}}{K_E} = \frac{[h_M^x h_O^y]}{[h_M^x h_O^y]_E} = \frac{[\%M]^x[\%O]^y}{\{[\%M]^x[\%O]^y\}_E} \tag{5}$$

K_{MO} is the solubility product of the oxide. The free energy balance for the nucleation of an oxide precipitated in the homogeneous melt includes the volumetric free energy and the surface energy opposing to the stabilization and growth of the nucleus,

$$\Delta G = 4\pi r^2 \sigma_{PL} + \left(\frac{4}{3}\right)\pi r^3 \Delta G_V \tag{6}$$

Making zero the derivative of the free energy (**Table 1** [26, 27] reports the molar Gibbs free energy of deoxidation reactions of iron melts) allows the calculation of the critical radius for the onwards growth of the nucleus, obtaining,

$$r_c = \frac{-2\sigma_{PL}}{\Delta G_V} = \frac{2\sigma_{PL}V_O}{RTlnS_0} \tag{7}$$

The free energy required for the nucleation is obtained by substituting this radius in Eq. (6),

$$\Delta G = \frac{16\pi\sigma_{PL}^3}{3\Delta G_V^2} = \frac{16\pi\sigma_{PL}^3 V_O^2}{3(RTlnS_0)^2} \tag{8}$$

The nucleation rate is [26, 28],

$$I = exp\left[\frac{16\pi\sigma_{PL}^3 V_O^2}{3k_B R^2 T^3 (ln\,S_O)^2}\right] exp\left(\frac{-\Delta G}{k_B T}\right) = A\,exp\left[\frac{-16\pi\sigma_{PL}^3 V_O^2}{3k_B R^2 T^3 (ln\,S_O)^2}\right] \tag{9}$$

$$A = exp\left[\frac{16\pi\sigma_{PL}^3 V_O^2}{3k_B R^2 T^3 (ln\,S_O)^2}\right] \tag{10}$$

where $k_B = 1.38 \times 10^{-23}$ J K^{-1}, is the Boltzmann constant, $A = 10^{32}$ m^{-3} s^{-1} is the frequency factor, V_O is the oxide's molar volume, σ_{PL} is the interfacial tension

Reaction	log K$_{eq.}$ (at 1873 K)
Al$_2$O$_3$ (s) = 2 $\underline{Al}$ + 3 $\underline{O}$	−55.76 (= 11.80–62790/T)
ZrO$_2$ (s) = $\underline{Zr}$ + 2 $\underline{O}$	−36.24 (= 21.76–57000/T)
MgO (s) = $\underline{Mg}$ + $\underline{O}$	−32.85 (= 12.45–38050/T)
SiO$_2$ (s) = $\underline{Si}$ + 2 $\underline{O}$	−19.39 (= 11.58–30400/T)
MnO (s) = $\underline{Mn}$ + $\underline{O}$	−5.55 (= 6.70–15050/T)
CaO (s) = $\underline{Ca}$ + $\underline{O}$	−42.76 (= 7.77–33700/T)

Table 1.
Equilibrium constants [26, 27].

between liquid iron and an oxide particle, R is the gas constant, and T is temperature. The critical supersaturation S_O^* is the minimum one to nucleate one nucleus $m^{-3} s^1$. Hence, making I = 1 $m^{-3} s^{-1}$ in Eq. (9) implies $S_O^* = S_0$, and gives,

$$S_0 = exp \left[\frac{V_0}{RT} \sqrt{\frac{16\pi\sigma_{PL}^3}{3k_B T ln A}} \right] \qquad (11)$$

The supersaturation of iron melts in contact with different oxides was measured through electrochemical methods [29]. The critical supersaturation, S_O^*, depends on the oxide's nature and surface tension, as seen in the precedent equation. The experimental results provide the inclusions sizes' statistical dispersion directly in the sense that the larger surface tensions, contributing to the opposing free surface energy to the nucleation, lead to larger size dispersions [26]. **Table 2** shows the experimental results of supersaturation experiments reported in Ref. [26] using different metal deoxidizers. The second and third columns are the molar volume and the interfacial tension between the oxide and the melt, the fourth and fifth, the experimental and calculated critical supersaturations through Eq. (11). The sixth and seventh columns include the experimental and corrected supersaturations, respectively. Revision of these data shows that the magnitudes of the calculated critical supersaturations are larger than the experimental critical supersaturations. The other observations are the small magnitudes of the experimental supersaturation. The large differences behind the critical supersaturations are due to the experimental data's nature as they correspond to the metal bulk property. On the other hand, the other magnitude (the corrected supersaturations) is theoretically related to the nuclei's curvature, as is schematized in **Figure 1**. The curvature raises the gradients of concentration of all solutes, M (Al, Si, Mn, Mg, Ti, Zr, Ca) and O in the nuclei's tip and, consequently, the critical supersaturations are larger in the proximities of the tip than in the metal bulk. The curvature, given by r_C^{-1} is calculated through Eq. (7) and matching its magnitude by considering an embryo formed by two or three pairs of M-O dimers, (consulting for that purpose the atomic radius of the involved elements of the corresponding oxides in the Periodic Table).

The correction of the experimental supersaturations is possible through the Gibbs–Thomson's Equation which gives the ratio between both types of supersaturations as,

$$[S_{0,corr}]_{r=r} = [S_{O,exp}]_{r=\infty} exp \left[\frac{V_0}{RT} \frac{2\sigma}{r_c} \right] \qquad (12)$$

OXIDE	Vo [m³. Mol⁻¹]	σ_{PL} [J. m²]	$S^*_{O\ (exp.)}$	$S^*_{O\ (cal.)}$	S_O	$S^*_{O\ (exp.)}$ corr	S_O corr.
MgO	1.10E-05	1.8	8.4	280	3.6 ∼ 7.2e4	280.224	1801440
ZrO₂	1.01E-05	1.63	4.5	85	48 ∼ 68	84.825	1093.3
Al₂O₃	8.60E-06	2.11	14.7	529	37 ∼ 60	530.229	1803.5
CaO	1.65E-05	1.17	3.4	83			
CaO-Al₂O₃	1.47E-05	1.3	3.6	92	8.5E+04	90.936	2147100
SiO₂	1.13E-05	1.24	1	27			
MnO-SiO₂	1.36E-05	1	1.7	18	1.5	18.598	16.41

Table 2.
Experimental, calculated and corrected critical supersaturation degree for precipitation of oxides [26].
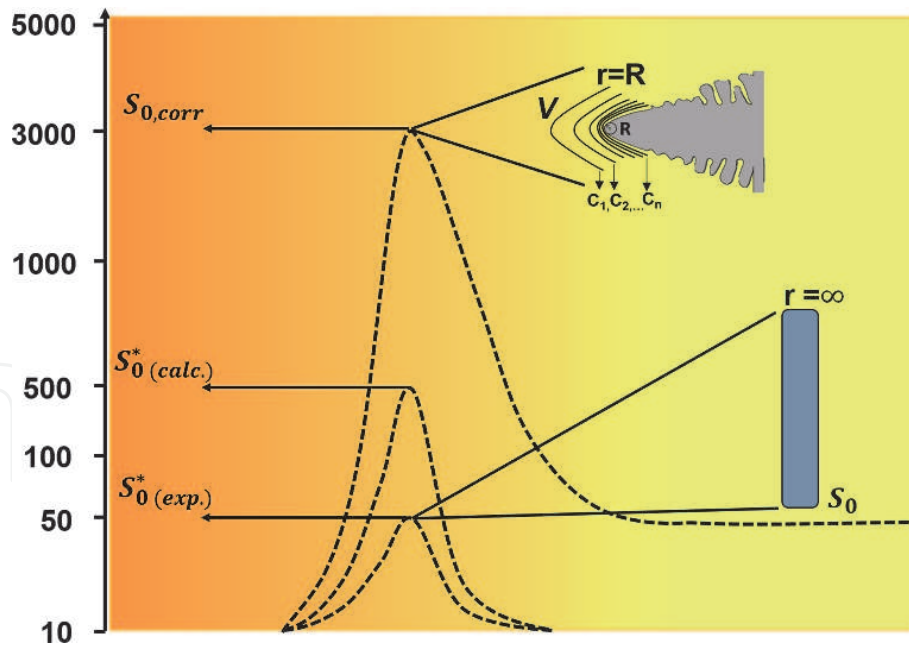
Figure 1.
Supersaturations of alumina close and far away from surfaces with finite and infinite curvature radius.

The nucleation process consumes short times of the order of microseconds [26, 29, 30], as shown schematically by **Figure 2.** The fluctuations of concentrations in the liquid structure, after the de-oxidant addition, require a critical supersaturation reached in the point (a) of this figure. Once reached the critical supersaturation, the embryo starts with a group of M-O dimers that develop into metastable structures becoming into a nuclei, and as the thermodynamic and kinetic conditions permit it, evolves in alumina with time, as seen in **Figure 3**. After stabilizing the nuclei, the local supersaturation decreases by diffusion process [31], due to the local consumption of M and O, to the point (b) in **Figure 2** where the nucleation kinetics overlaps with the diffusion process. The supersaturation continues decreasing and the
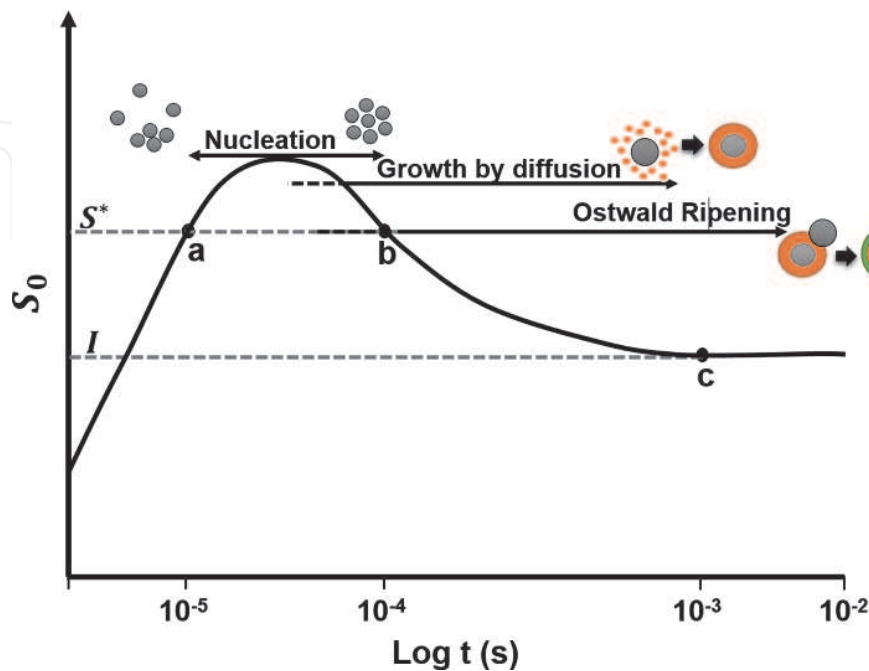

Figure 2.
Evolution of supersaturations with time during nucleation and initial growths by diffusion and Ostwald ripening mechanisms.

5

diffusion overlaps with the particle growth through the Ostwald ripening process summarized by the following expression [32],

$$\acute{r}^3 - \acute{r}_0^3 = \alpha k_d t \qquad (13)$$

$$k_d = \frac{2\sigma D_O V_O C_O}{RT(C_P - C_O)} \qquad (14)$$

where C_O and C_P are the concentrations of dissolved oxygen and oxygen content in the oxide, respectively, and D_O is the diffusion coefficient of oxygen. Further growth phenomena of the particles, in industrial vessels, includes Stokes collisions, collisions among particles driven by turbulent flows deriving in aggregates of particles and clusters. Grown particles are easily floated out thanks to the bottom stirring with argon of steel ladles which carries these particles through their contact with gas bubbles, and melt convection making them contact the slag facilitating their absorption in this phase.

Figure 4a and **b** show the effect of the supersaturation on the nucleation kinetics on the nucleation rates of different oxides recalculated from reference [26]. There are two important differences, the first is that the nucleation rates are considerably lower than those reported in Ref. [26] and the second is the larger supersaturations required to precipitate the MgO shown in **Figure 4b**. Another important feature is the small supersaturations required for the precipitation of silica and manganese silicate. Therefore, those particles requiring small or relatively small supersaturations yield the largest nucleation rates meaning, physically, the fast generation of million of nuclei distributed inside the reaction and diffusion boundaries.
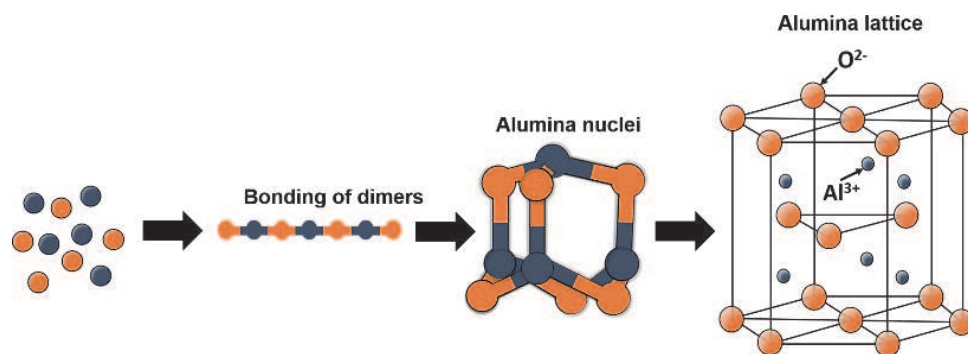

Figure 3.
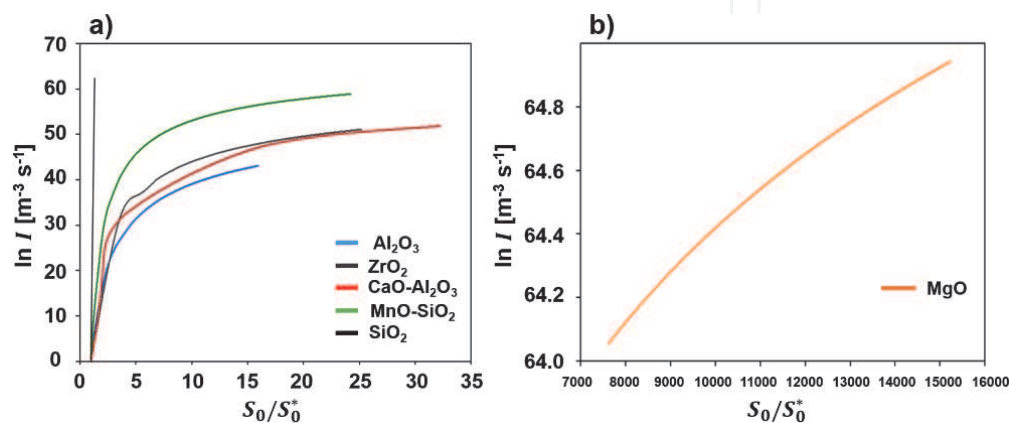*Nucleation of an alumina lattice from the union of Al-O dimers.*

Figure 4.
Effect of supersaturation ratios on nucleation rate at 1600°C, (a) various metal deoxidizers, (b) with magnesium.

The main obstacle of a particle to born is the creation of a new surface preceding the formation of a small volume in a hosting matrix, as is seen in **Figure 3**, with a different structure. Those particles requiring larger supersaturations would, eventually, nucleate smaller populations of particles with a broader size distribution once their first step of development ends. The precipitates characterized by high and low supersaturations are schematized in **Figure 5a** and **b**, respectively, showing the period for each one of them. The first case will yield numerous small particles with limited growth as the supersaturation decays providing a narrow size distribution. The longer times lead to larger diffusion and growth time scales yielding broader size distributions in the second case. The time scales change to exponentially larger ones when the precipitates of solid-state transformations take place. For example, steel aging by nitrogen diffusion consumes long times as the diffusion coefficients of this interstitial element are very small in ferrite or austenite phases at 300°C [32, 33] compared with its diffusion coefficient at 1600°C [34], as is schematized in **Figure 5c** and **d.** Hence, the interfacial tension between the melt and the nuclei governs the nucleation rate, as seen in **Figure 6**. Alumina has one of the lowest nucleation rates as its interfacial tension is large, and its crystals will have a broad spectrum of sizes after the nucleation and the diffusion end.

2.2 Alumina morphology

Alumina may acquire a wide diversity of morphologies depending on the concentrations of oxygen and the deoxidant. Accordingly, the initial supersaturation ratio influences the morphology of alumina. **Figure 7** shows a scheme of the relation between oxygen concentrations and the deoxidant with the particle morphology [35]. In oxidized melts, the inclusions are rounded spheroids, as the oxygen activity decreases the surface roughness develops reaching the stage of dendritic precipitation. With further deoxidation the morphology changes to faceted, disks and crystalline rhomboids.

The heterogeneous nucleation of alumina particle also yields characteristic morphologies. Other foreign particles catalyze alumina's nucleation in the melt, such as those of metastable iron oxide precipitated in the steelmaking furnace and manganese silicates in the refining ladle [36]. A catalyzed nucleation process means that
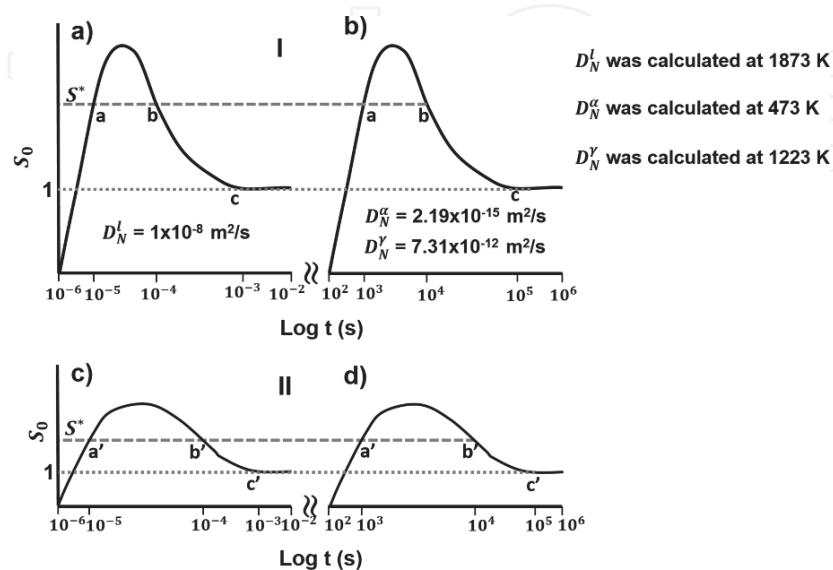

Figure 5.
Schematics of nucleation rate evolution with time. (a) High nucleation rates at low supersaturation in liquid state, (b) high nucleation rates in solid state, (c) low nucleation rates at high supersaturation in liquid state, (d) low nucleation rates in solid state.
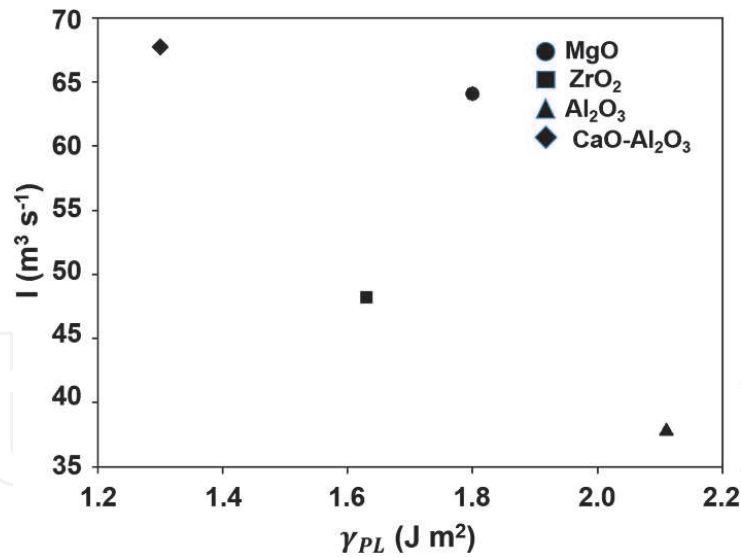
Figure 6.
Nucleation rate as a function of surface tension between the particle and the melt at 1600°C.
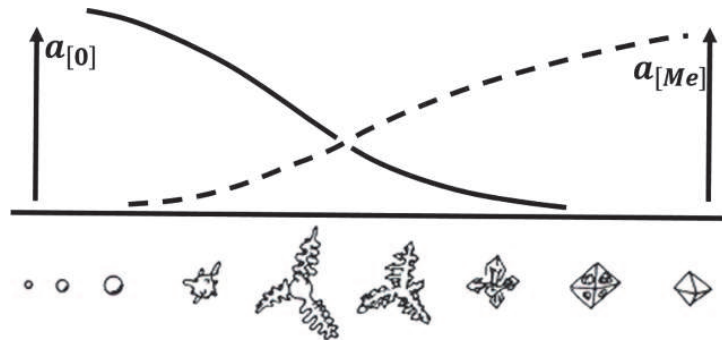

Figure 7.
Evolution of the growth shapes of oxide inclusions as a function of the local oxygen activity (solid line) and deoxidizer activity (dashed line) according to Steinmetz [35].

the foreign particle decreases the supersaturation required by the precipitation process of the particle through a decrease of the free energy according to [32],

$$\Delta G_{het} = \left\{ \frac{-4}{3} \pi r^3 \Delta G_v + 4\pi r^2 \sigma_{PL} \right\} S(\theta) \tag{15}$$

where

$$S(\theta) = \frac{(2 + cos\theta)(1 - cos\theta)^2}{4} \tag{16}$$

Note that except for factor $S(\theta)$ this expression is the same as that obtained for homogeneous nucleation, Eq. (6). $S(\theta)$ has a numerical value ≤ 1 dependent only on θ, i.e. contact angle and the nucleus's shape. A catalyzed alumina particle will have a morphology depending on the oxide's nature over which it nucleates as shown in **Figure 8** [36]. If the foreign o catalyzer particle is a silicate, already existent given its high nucleation rate, a chemical reaction intervenes,
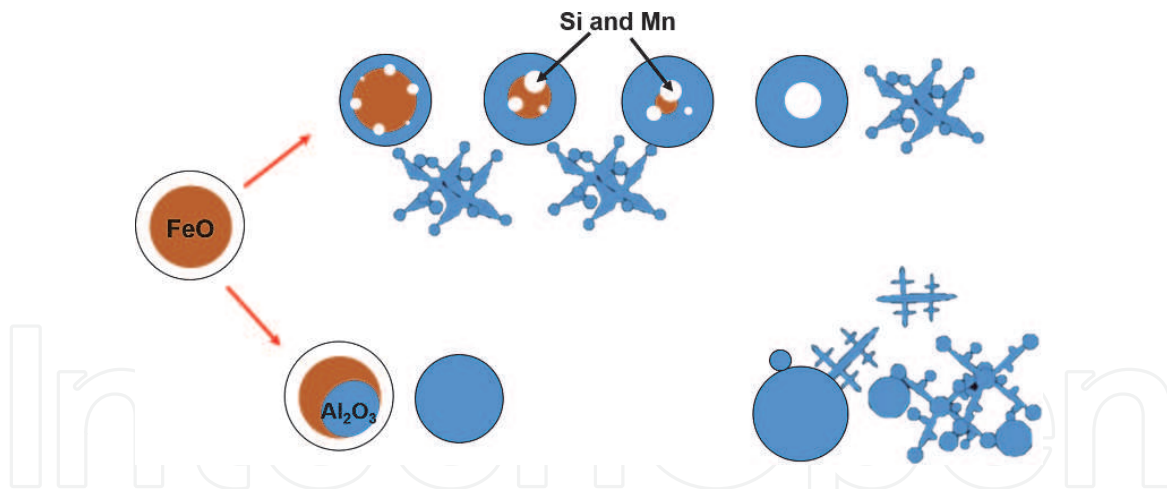
$$2[Al] + (MnO \bullet SiO_2) = (Al_2O_3) + [Mn] + [Si] \tag{17}$$
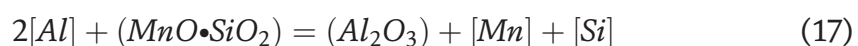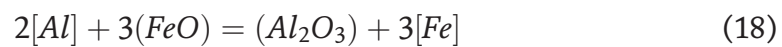
if the particle is iron oxide, then

Figure 8.
Heterogeneous nucleation of alumina on iron oxide and silicate particles [36].

$$2[Al] + 3(FeO) = (Al_2O_3) + 3[Fe] \tag{18}$$

The interfacial tension between the alumina and silicate particles is reduced due to the chemical reaction, a layer of alumina, (it is initially nucleated and the alumina layer grows by the reaction), surrounds the particle of silicate making sluggish the diffusion of aluminum through the alumina layer to continue the reaction. During the process, some particles of Mn and Si precipitate as products of the reaction (17). No dendrites were observed and there is the presence of needle like clusters with disk type terminations indicating a growth under small supersaturations, once the oxygen content decreases. Iron oxide suffers a rapid reduction by aluminum, reaction (18) and the product is an alumina particle without other phases. Other alumina particles nucleate heterogeneously on the original alumina particles and yield dendritic morphologies.

2.3 Further growth of inclusions

After concluding the nucleation and growth by diffusion and Ostwald ripening, the inclusions continue their growth through direct collision. In a Stokes flow regime, the probability for collision among inclusions of sizes R_1 and R_2 is [37],

$$w_s = \frac{2}{9}g\frac{\Delta\rho}{\mu}|R_1 - R_2|(R_1 + R_2)^3 \tag{19}$$

and the probability of collision under the action of turbulent eddies is expressed by the Saffman's Equation as [38],

$$w = 1.3\sqrt{\pi}(R_1 + R_2)^3\sqrt{\varepsilon/\nu} = 7.2|R_1 - R_2|(R_1 + R_2)^3\{Noexp(-\alpha R_1)Noexp(-\alpha R_2)\}/2 \tag{20}$$

In Stokes regime, the highest collision probability is observed when the inclusions have large size differences as seen in **Figures 9** and **10** indicates that collisions of silicate inclusions smaller than ten μm, have low probabilities for collisions under turbulent flow conditions and those with large dimensions have higher collision probabilities. **Figure 11** shows the corresponding collision probabilities for alumina inclusions and particles as small as three μm yield the highest probabilities for a collision. Therefore, alumina inclusions grow from microscopic inclusions to large aggregates and clusters by collisions among small particles forming aggregates [40].
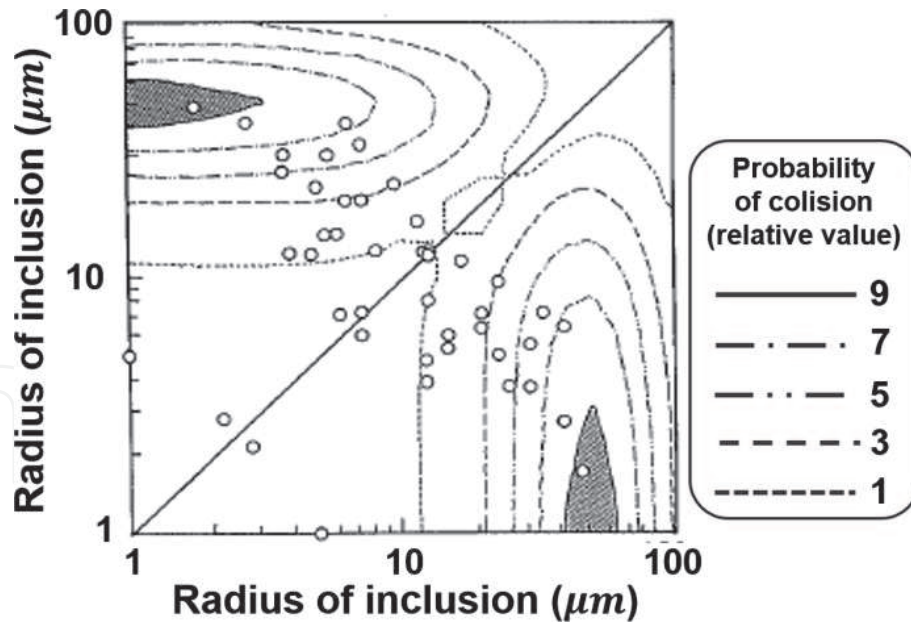
Figure 9.
Comparison of the collision probability (Stoke's model) with the radius of the inclusions. Miki Y, Kitaoka H, Sakuraya T, Fujii T. mechanism for separating inclusions from molten steel stirred with a rotating electro-magnetic field. ISIJ Int. 1992;32:142–149. DOI: 10.2355/isijinternational.32.142. Reproduced with permission [39].

Figure 10.
Comparison of the collision probability (Saffman's model) with the radius of the inclusions. Miki Y, Kitaoka H, Sakuraya T, Fujii T. mechanism for separating inclusions from molten steel stirred with a rotating electro-magnetic field. ISIJ Int. 1992;32:142–149. DOI: 10.2355/isijinternational.32.142. Reproduced with permission [39].
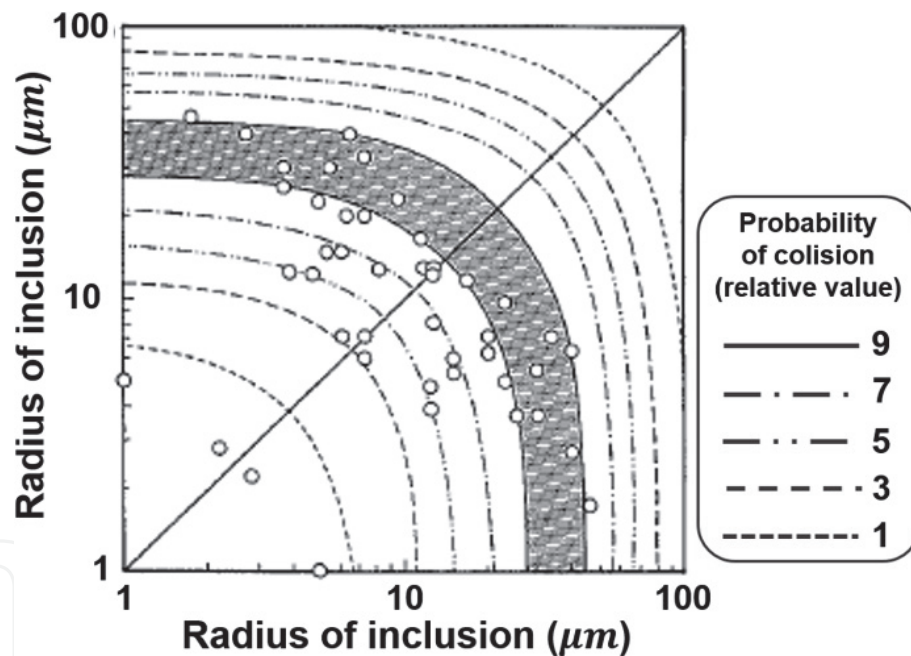
Roughly speaking, in the turbulence regions, in a bottom stirred ladle, the ratio between Stokes and Safmann's regimes is approximately 6×10^4. Thereby, deoxidation during steel tapping in bottom stirred ladles is the most indicated step to deoxidize and grow inclusions by turbulent collisions. This is particularly applicable to the growth of alumina particles. Indeed, vigorously stirred melts at tapping times, lead to cleaner steel heats [41]. In the secondary refining of steel, where the turbulence levels are considerably smaller, this ratio decreases and is the highest in the argon-plume regions, while in the top layer of the bath, the Stokes regime dominates.
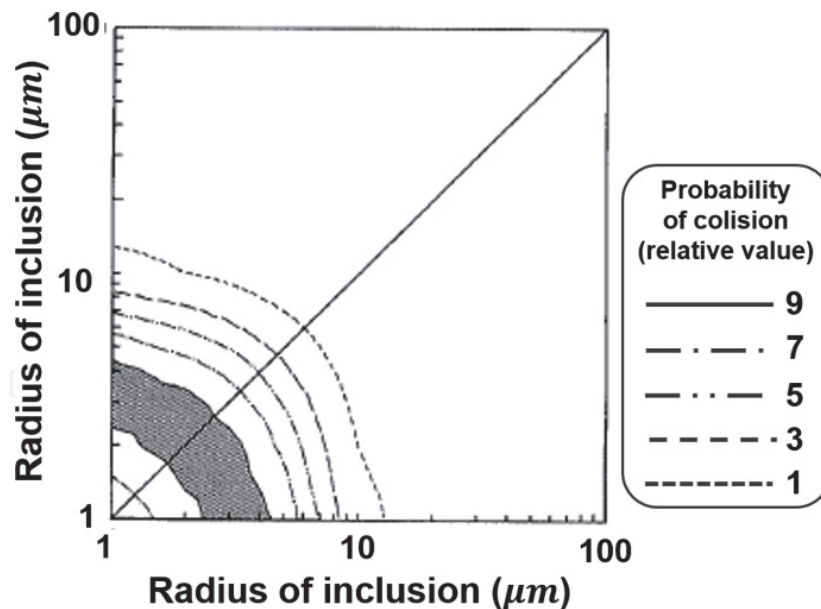
Figure 11.
Prediction of the collision probability (Saffman's model) for alumina inclusions. Miki Y, Kitaoka H, Sakuraya T, Fujii T. mechanism for separating inclusions from molten steel stirred with a rotating electro-magnetic field. ISIJ Int. 1992;32:142–149. DOI: 10.2355/isijinternational.32.142. Reproduced with permission [39].

2.4 Bond strength among particles

Another important aspect of inclusions growth is the stability of aggregates and clusters, forming large particles that float out of the bath faster as larger are their sizes. Strong bond strengths are desirable as once the particles form aggregates or clusters, their integrity must prevail, avoiding the generation of smaller particles, by breaking processes due to turbulence, which may bring on floatation slowness. The variety of bonds among inclusions with a wide spectrum of morphologies is simplified into three basic cases, sphere-sphere, sphere-plate and plate-plate, see **Figure 12**. According to thermodynamic calculations of surface tensions, the plate-plate geometry yields the largest bond strength, as suggested by **Figure 13** [42]. The bond strength, eventually, will increase by the thickenings of the neck formed by the union of two particles of alumina through diffusion processes according to,

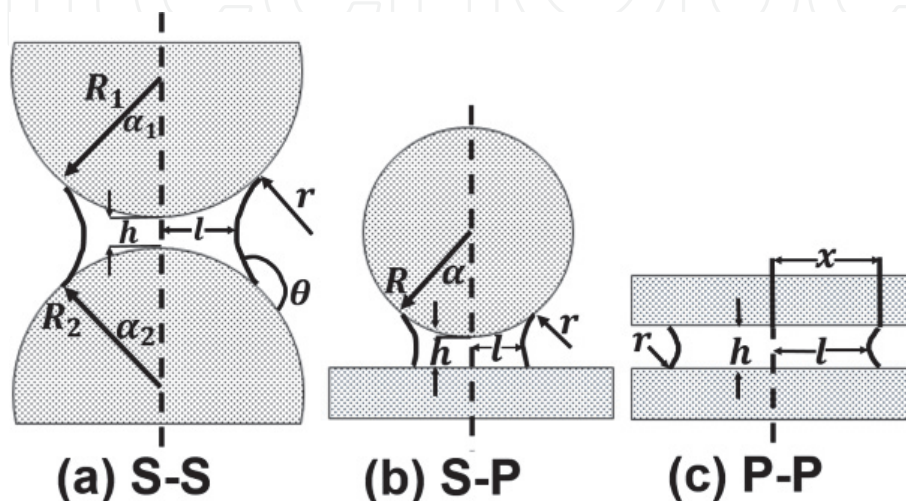$$\frac{x^5}{R^2} = \frac{K_1 \sigma_{PP} V_0}{RT} D_V t \qquad (21)$$

(a) S-S   **(b) S-P**   **(c) P-P**

Figure 12.
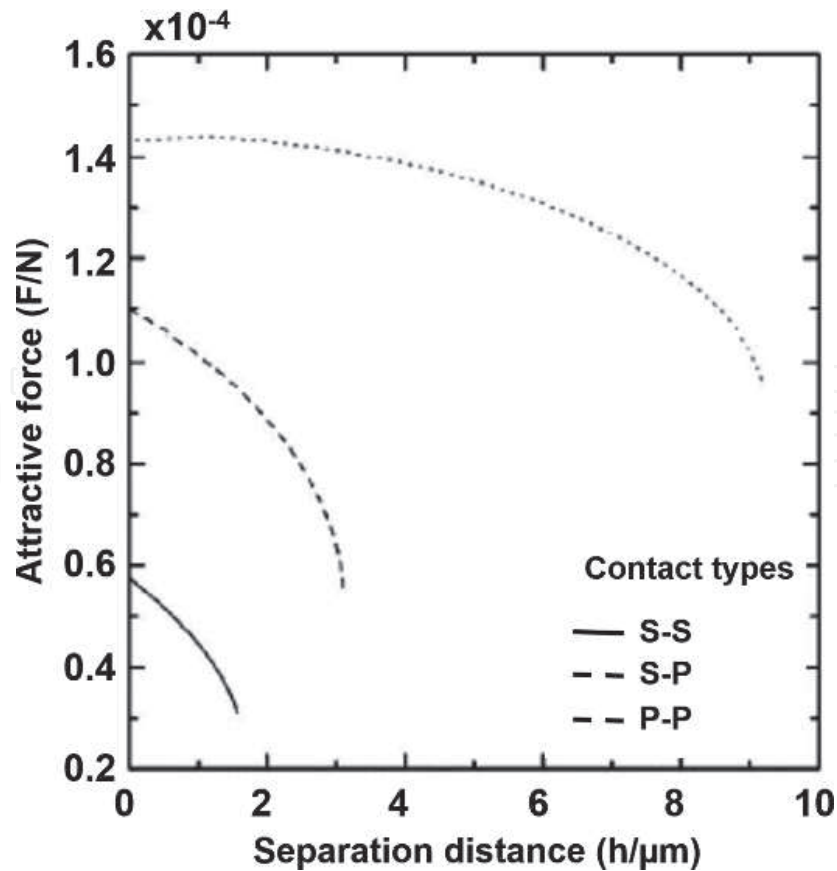*Geometries of the gas cavity of different contact types [42].*

Figure 13.
Attractive force for different contact types. Zheng L, Malfliet a, Wollants P, Blanpain B, Guo M. effect of alumina morphology on the clustering of alumina inclusions in molten iron. ISIJ Int. 2016;56:926–935. DOI: 10.2355/isijinternational.ISIJINT-2015-561. Reproduced with permission [42].

In this equation, $D_V = 1.3X10 \, exp \left(\frac{-110000}{RT} \right)$ [43], $\sigma_{pp} = 1 \frac{J}{m^2}$ is the interfacial tension between alumina particles $K_1 = 10$–100 [43]. **Figure 14** shows the mechanism of diffusion of vacancies in the alumina lattice to form the bond [44]. The bond strength reaches the order of MPa due to the interdiffusion between alumina particles [45].

3. Adherence of alumina particles on refractory surfaces

The adhesion of alumina inclusions to the refractory surface has its highest repercussion in the nozzle feeding with liquid steel the continuous casting slab mold. The property governing these phenomena is the contact angle between a particle and a solid phase with a smooth surface as is shown in **Figure 15**, which is a function of the surface tension and known as Young's law [47],

$$\sigma_{SL} = \sigma_{SV} - \sigma_{LV} \cos \theta_Y \tag{22}$$

In actual refractory materials, there are not smooth surfaces and have certain levels of asperities and roughness. Hence, Eq. (22) suffers a modification through a roughness factor, r, to become in the Wenzel's Equation [47],

$$\cos \theta_W = r cos \theta_Y \tag{23}$$

A further modification includes the consideration of the heterogeneous structural nature of industrial materials such as refractories for continuous casting and Eq. (23) becomes into the Cassie-Baxter Equation [47],
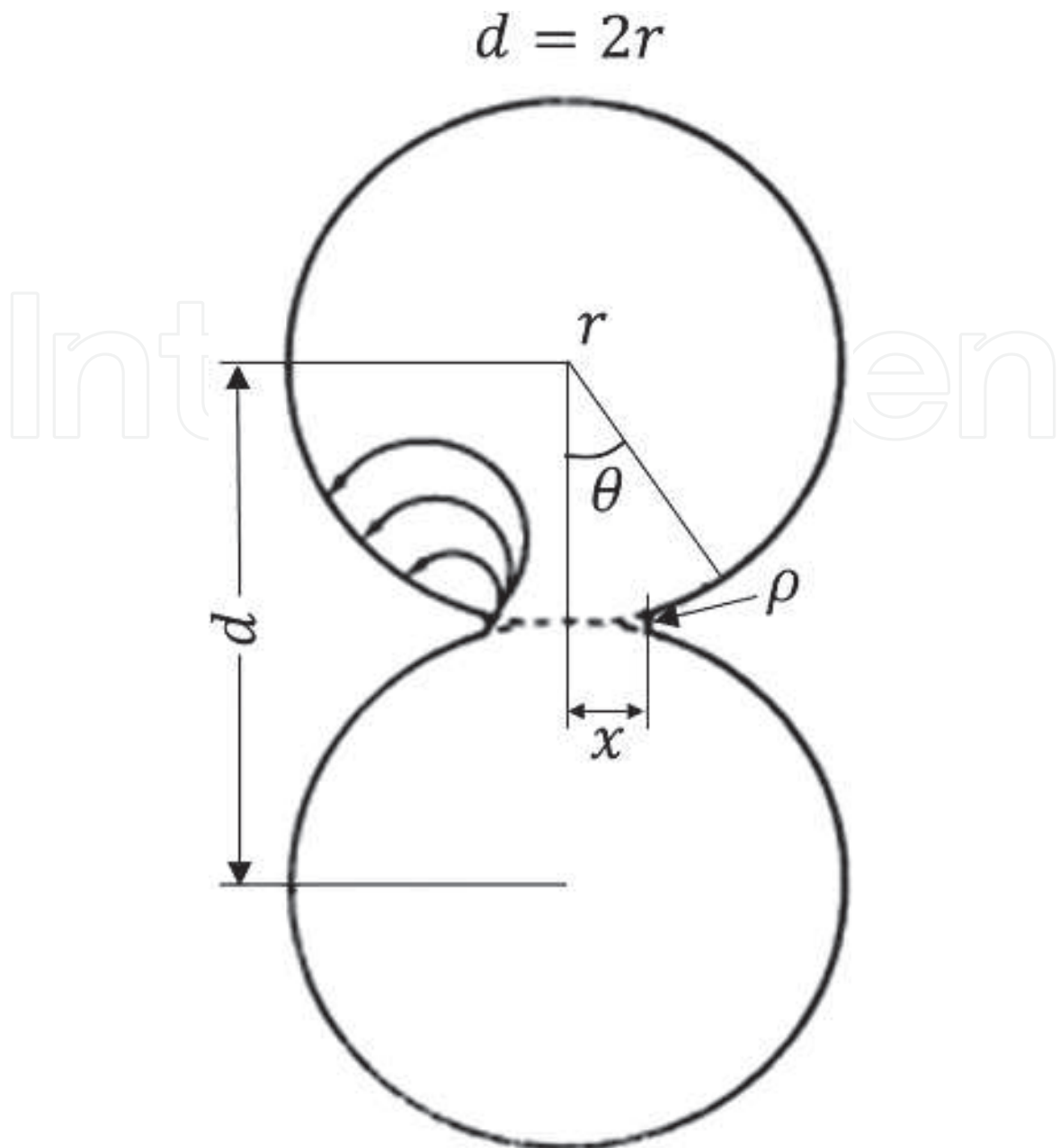
Figure 14.
Models for initial stages of sintering of spherical particles showing the vacancies diffusion paths [43].
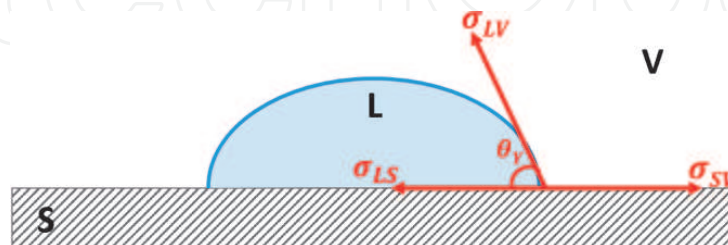

Figure 15.
Contact angle between surfaces in a liquid in equilibrium with a vapor phase [46].

$$\theta_{CB} = \frac{\sum_{i=1}^{n} f_n (\sigma_{i,SV} - \sigma_{i,SL})}{\sigma_{LV}} \tag{24}$$

Where the limits i and n, in Eq. (24), corresponding to the stable phases forming part of the refractory material and f_i is the surface fraction of phase i. The following

conditions establish the wettability conditions: when $\sigma_{SV} > \sigma_{SL}, 0^0 < \theta_{CB} < 90^0$, the liquid wets the solid. When $\sigma_{SL} > \sigma_{SV}, 90^0 < \theta_{CB} < 180^0$, the solid and the liquid have a poor wettability. The work of adhesion between a particle and a substrate is derived from Young's Equation,

$$W_{ad} = \sigma_{SV} + \sigma_{LV} - \sigma_{SL} = \sigma_{LV}(1 + cos\,\theta_{CB}) \tag{25}$$

A specific case of changes of surface tension of liquid steel is the case of ultra-low carbon steels stabilized with Ti (Ti-SULC steels) where this element decreases this property as seen in **Figure 16a**, and the work of adhesion as a function of the Ti content is shown in **Figure 16b** [46]. This effect of Ti on the surface tension of Ti-SULC steels enhances the wettability between the melt and the inclusions. The wettability of hydrophilic and hydrophobic systems (such as steelmaking and casting processes) increases and decreases, respectively, with surface roughness, leaving behind the ideal behavior, indicated by Young's Equation, as the best condition. **Figure 17a** shows the effects of the surface roughness on the contact angle or Wenzel angle. Increasing the roughness ratios make a hydrophilic system more hydrophilic and a hydrophobic system in a more hydrophobic one. It can be assumed that in the actual metal-refractory contact, due to poor wettability between the two phases, a gas can be trapped in between the asperities of the surface, such that the liquid sits on a surface having a distribution of solid asperities and gas pockets (two-component surface material) and their surface fractions are f_S and f_V respectively, where $f_S + f_V = 1$. Substituting in the CB Equation for the solid–liquid fraction $f_1 = f_S$ and $cos\,\theta_{CB.1} = cos\,\theta_{CB,2}$ and the gas pocket fraction $f_2 = f_V$ and $cos\,\theta_{CB,2} = -1$ because the fraction is completely dry (no-wetting) and combining the roughness ratio factor r with the CB Equation, we get

$$cos\,\theta_{app} = rf_S\,cos\,\theta_{CB} + f_S - 1 \tag{26}$$

The examination of Eq. (26) indicates that if the fraction f_S approaches 0, by increasing the asperities of the surface, there will be a condition of perfect non-wettability. This trend is shown in **Figure 17b**. On the contrary, if f_S approaches 1 (complete surface smoothness), the contact angle is given by Eq. (26) with r = 1. The combined effects of roughness and a solid fraction are as follows: in a hydrophilic system, the simultaneous increases of solid fraction and surface roughness make a hydrophilic system more hydrophilic. A decrease of the solid fraction with a combined increase of surface roughness makes this hydrophobic system in a more

Figure 16.
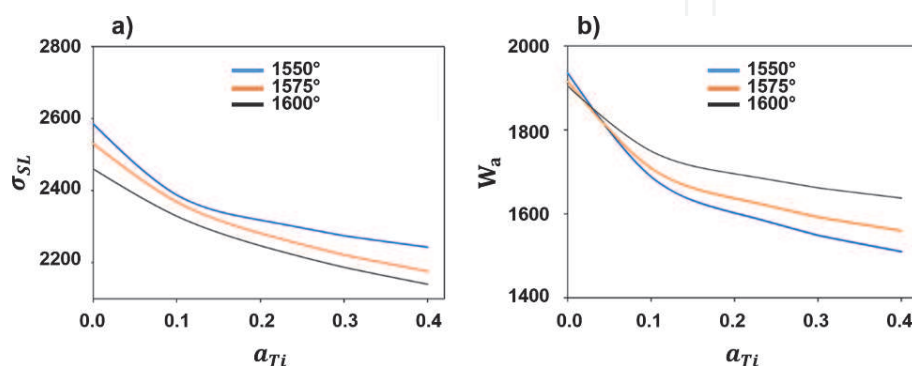*Interfacial properties between liquid steel containing Ti and alumina particles, (a) interfacial tension, (b) adhesion work. González-Solórzano M.G., Morales R.D. Gutiérrez E, Guarneros J, Chattopadhyay K. analysis of fluid flow of liquid steel through clogged nozzles: Thermodynamics analysis and flow simulation. Steel. Res. Int. 2020;91. DOI: 10.1002/srin.202000049. Reproduced with permission [46].*

Figure 17.
Effect of roughness and voids on the surface refractory on interfacial properties, (a) comparison between Wenzel's and Young's equation, (b) effect of solid fraction for contact points according to the Cassie-Baxter equation. Of fluid flow of liquid steel through clogged nozzles: thermodynamics analysis and flow simulation. Steel. Res. Int. 2020;91. DOI: 10.1002/srin.202000049. Reproduced with permission [46].
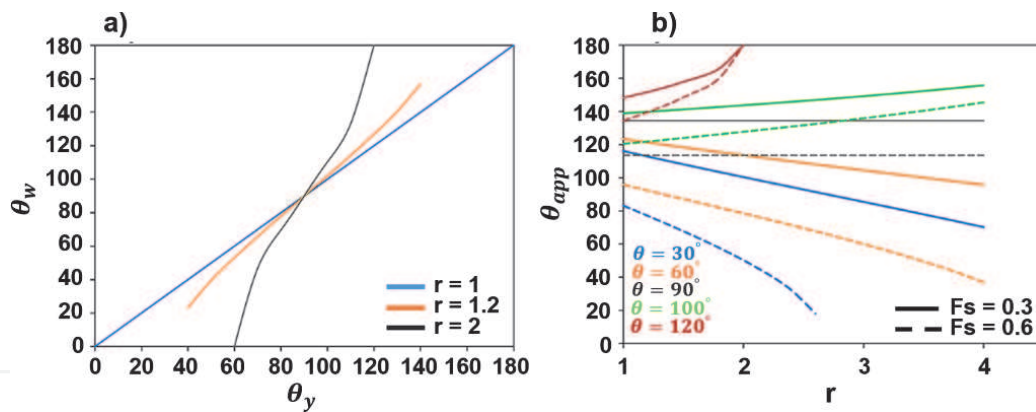
hydrophobic one. Decreasing the adherence of inclusions on the refractory surface requires two simultaneous conditions that must be fulfilled: a small contact angle between the melt and the inclusion and a low contact angle between the refractory and the melt. Therefore, to manipulate the second angle, there may be two ways:

1. The first is to use CaO as a surface cover, which would be wetted it by liquifying the alumina inclusions and decreasing the contact angle between the melt and the calcium aluminate inclusion.

2. Use a conventional AG material with a special treatment leading to smooth surfaces according to the results presented in **Figure 17**.

The changes of wettability among the refractory, the melt, and the inclusions are summarized in **Figure 18(a–d)**:

a. The contact angle 1 (between the inclusion and the melt) is larger than the contact angle 2 (between the refractory and the melt). Hence, the liquid does not wet the nozzle. Therefore, the refractory rejects the metal, and there is the adhesion of the inclusion to the wall.

b. When the contact angle 2 is larger than angle 1, the nozzle is slightly wettable by the melt and allows that this one enters between the inclusion and the wall, making a small separation between them and reducing the strength of adhesion.

c. When angle 2 decreases further, the nozzle wall will increase its wettability by the melt. Hence, the separation between the inclusion and the wall becomes larger, making inclusion separate from the nozzle wall.

d. In this case, the liquid wets the inclusion; if the inclusion is liquid, it will go with the flow, but if it is solid, the inclusion approaches the wall and will remain adhered to it.

As the liquid steel flows through the nozzle, **Figure 19**, the alumina particles are transported along, and those close to the boundary layer might, eventually, get in this region and adhere to the refractory's surface by mechanisms of fluctuating velocities [48, 49]. Therefore, in current casting systems, the adherence of an
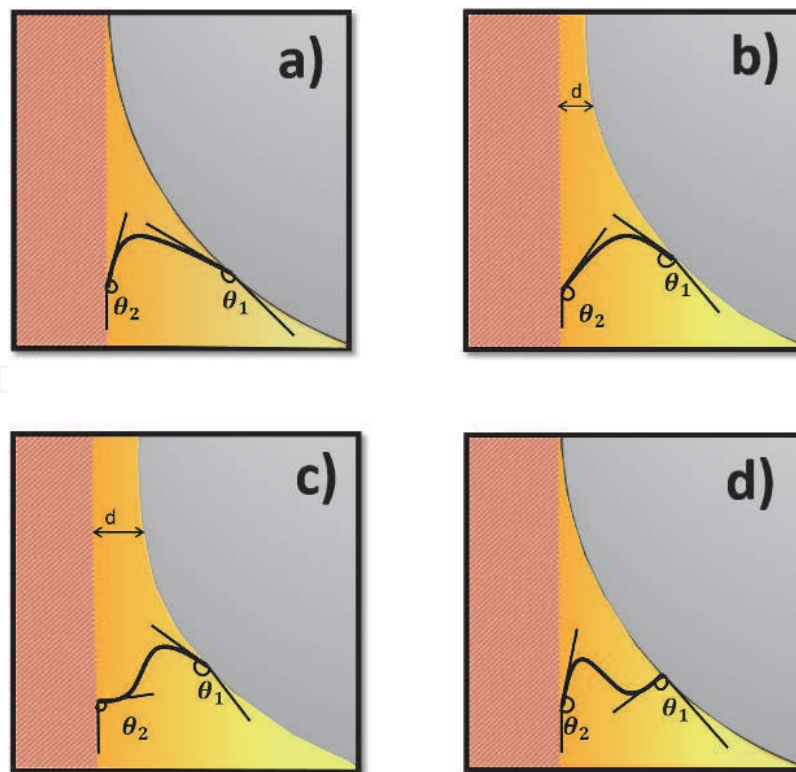
Figure 18.
Effects of melt-refractory and melt-inclusion contact angles on particle-refractory surface adhesion.

alumina particle to the surface of a nozzle refractory is favored by the low wettability of the inclusion and the refractory by the melt.

3.1 Adherence force

When a particle approaches the solid surface or to another particle, both unwetted by the liquid, the formation of a cavity between them becomes thermodynamically favorable, see **Figure 20**. This phenomenon is because the replacement of a particle-liquid interface by a particle-vapor interface leads to a negative change of the Gibbs free energy according to Young's Equation. Once the cavity is formed, an attractive force of adhesions develops, F_A, as expressed in the following Equation [50],
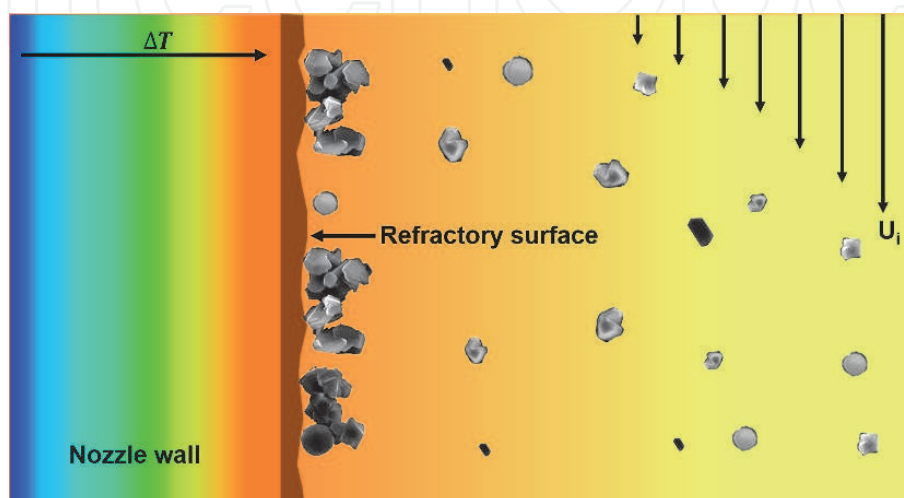

Figure 19.
Adhesion of alumina clusters and aggregates contained in the liquid flow on the nozzle surface.
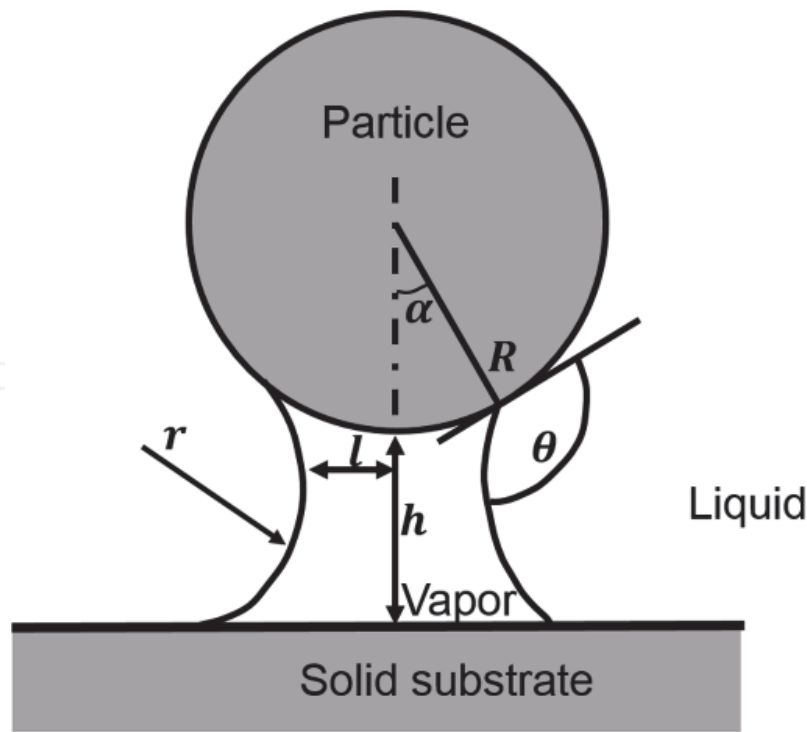
Figure 20.
Schematization of a cavity between a sphere and a plate in a non-wetting system.

$$F_A = 2\pi\sigma_{LV}l + \pi l^2 \Delta P \tag{27}$$

The cavity might be filled with: (1) gaseous components initially dissolved in the melt (2) gaseous components coming from the refractory (3) melt vapor, or (4) liquid phases forming due to a local rise in the oxygen concentration. In any case, there will be a pressure drop between the liquid outside of the cavity and the phase inside of it. The pressure difference obeys Laplace's Eq. (45),

$$\Delta P = \sigma_{LV}\left(\frac{1}{r} - \frac{1}{l}\right) \tag{28}$$

Where l and r are the principal radii of the cavity. The two parameters determine the profile of the liquid–vapor interface, which can be either optimized using the Laplace-Young Equation at constant pressure drop or approximately described with a piece of a circle with radius r. When the cavity is in equilibrium with the liquid phase, its shape is determined by thermodynamics. The estimated adhesion force between an alumina particle and the wall of an AG (alumina-graphite nozzle) is about 25×10^{-6} N [51], large enough to keep fixed the particle on the refractory surface.

4. Boundary conditions of wall adhesion

To design nozzle materials through the principles of physical-chemistry of interfaces and techniques of computer fluid dynamics, reliable boundary conditions for inclusion adherence to the refractory wall are necessary. In other words, to develop new materials is necessary to deal with a theoretical analysis including effects of surface roughness, the effect of impurities in alumina graphite materials (mainly Na_2O and K_2O, oxides cover) together with control of the boundary layer by the internal design of the nozzle [46] before making investments on experimental research. Specifically, this boundary condition is applicable only during the

development of the clog's first layer and not during its growth. That is to say, when the first layer of the clog stabilizes, its future growth is guaranteed by contact with other alumina particles, which will go through a sinterization process by diffusion of vacancies, as explained above, forming high strength bonds. This boundary condition is derived from a balance of forces, according to **Figure 21.** These forces obey the following expressions [52]:

Drag force

$$F_d = 6\pi\mu\gamma \frac{d_p^2}{4} f \tag{29}$$

Adhesion force

$$F_a = \frac{3}{4} \pi\sigma d_p \tag{30}$$

Buoyancy force

$$F_b = \left(\rho_L - \rho_p\right) g \frac{1}{6} \pi d_p^3 \tag{31}$$

Lift force

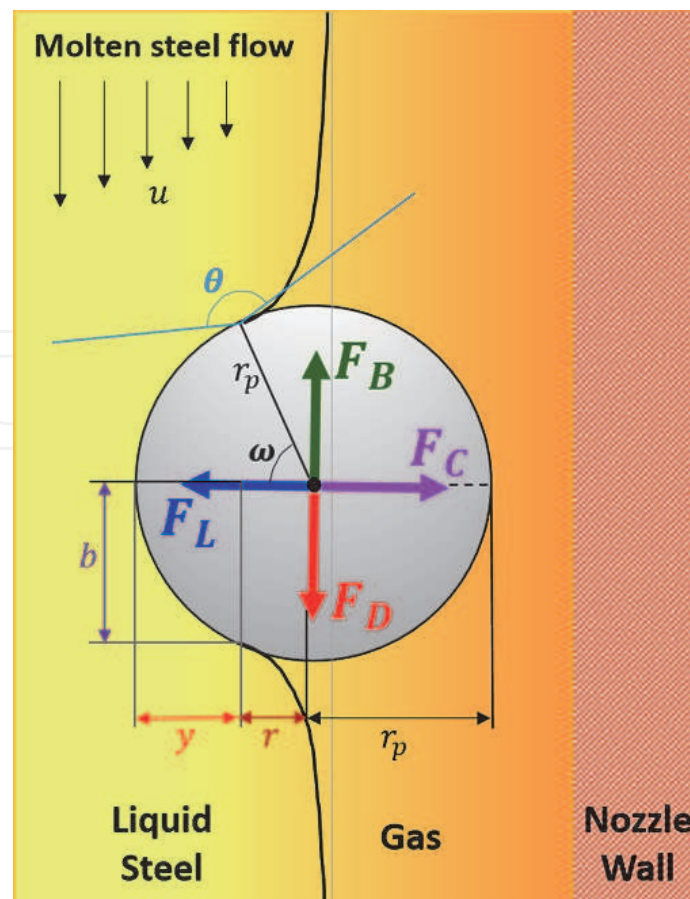$$F_L = 9.22 \frac{\gamma\mu d_p^2}{4} \frac{\gamma d_p^2}{4v} \tag{32}$$

Figure 21.
Forces acting on an inclusion. (FC = capillary force, FB = buoyancy force, FL = lift force, FD = drag force) [51].

Different force ratios working on the particles are useful as possible boundary conditions or, simply, to compare the magnitudes of these forces as follows:

Ratio for the vertical lift-off

$$R_v = \frac{F_L}{F_a} \tag{33}$$

Ratio for the sliding:

$$R_s = \frac{F_d + F_b}{k_s(F_a - F_L)} \tag{34}$$

Ratio for the tangential lift-off:

$$R_t = \frac{(1.4r_p)F_d + aF_L + r_pF_b}{aF_a} \tag{35}$$

The constants and variables included in these expressions are reported in **Table 3** [53]. In these calculations, instead of using Eq. (30) to estimate the adhesion force, the force suggested of 25×10^{-6} N was employed [51]. This force was calculated by optimizing Eq. (27) and Eq. (28) and is considered a more realistic magnitude. The force ratios calculated for a ten μm particle in a liquid steel flow are in the last column of **Table 3**. Some conclusions derived from these results are a) The lift force is negligible compared with the adhesion force. b) The ratio for sliding is small compared with the effects of the adhesion force. c) Summing the momentums of drag, lift, and buoyancy forces and compared with the adhesion force's momentum yields a magnitude larger than one, meaning that the particle may be dislodged from the wall.

Closure

The clogging phenomena have their roots in the deoxidation step of the liquid steel. Operational factors like the addition time of aluminum, oxygen supersaturation, temperature, and melt stirring fixe the initial conditions of sizes distributions

Parameters for the calculation of ratios [53]		
Shear rate, γ	$1 \times 10^5 \text{ s}^{-1}$	**Ratio of forces**
Poisson's ratio, v_1	0.27	$R_v = 5.12x10^{-8}$
Poisson's ratio, v_2	0.28	
Poisson's ratio, E_1	$8.01x10^{10}$	
Poisson's ratio, E_2	$2.15x10^{11}$	
Surface energy, σ	0.001 J.m^{-2}	$R_s = 0.064$
Coefficient of friction, k_s	0.3	
f	1.7009	
Viscosity, μ_l	0.006 Pa.s	
Liquid density, ρ_l	7100 kg/m^3	$R_t = 7.60$
Particle density, ρ_p	3600 kg/m^3	
Particle diameter, d_p	10×10^{-6} m	
Gravity, g	9.8 m/ s^2	

Table 3.
Parameters and constants to estimate the forces on a particle with a 10 μm diameter.

and the alumina particle's population responsible of the nozzle clogging. The high level of supersaturation required by aluminum governs the initial size distribution. Once the particle is nucleated at the initial stages, the initial growth is through diffusion and Ostwald ripening mechanisms. Although not proved yet here, the published literature reports that the bond strength among alumina particles and their morphology are important on the clogging mechanism. Once inside the nozzle, the particle, taking contact with refractory, may remain adhered to it if the adhesion force is larger than the momentums originated from the lift, buoyancy and drag forces with the particle size.

The refractory's roughness is of no help to control the clogging as those materials that are hydrophobic or hydrophilic will enhance these properties with rough surfaces. Ideally, a smooth surface approaching the Young's Law would be the ideal material to decrease clogging. Raw materials purity is of interest as some oxides are easily reduced by the carbon of the nozzle or aluminum in the melt, all working to enhance the clogging problem.

Under the present situation, this work contributes to the understanding of the surface phenomena in the areas of inclusion nucleation and growth of inclusions and the steel refining and the interaction with the refractory. It gives options for the boundary conditions applied in computational fluid dynamics simulations, all focused on designing new nozzle materials.

Nomenclature

C_O	Oxygen concentration in the melt
C_P	Oxygen concentration in the oxide
d_p	Particle diameter
D_O	Diffusion coefficient of oxygen in the melt
D_V	Coefficient diffusion of vacancies
f	Correction factor
F	Force
F_s, F_v	Surface fraction of solid and vapor phase, respectively
g	Gravity constant
h_i	Henryan activity of i
I	Nucleation rate
k_B	Boltzmann's constant
l	Principal radii
N_o	Constant
P	Pressure
r	Inclusion radii
r_0	Initial radii of the inclusion
r_c	Critical nuclei radii
R	Gas constant and particle radii
R_1	Particle 1 radii
R_2	Particle 2 radii
S_0	Supersaturation
t	Time
T	Temperature
V_O	Oxide molar volume
w	Collision probability of two particles in turbulent flow regime
W_{ad}	Work of adhesion
W_s	Probability for collisions for two particles in Stokes's regime
x	Neck radii

Greek letters

α	Accommodation factor
γ	Shear rate
ε	Dissipation rate of kinetic energy
θ	Contact angle
μ	Dynamic liquid viscosity
ν	Kinematic liquid viscosity
ρ	Density
σ	Surface tension

Sub indexes

a	Adhesion
app	Apparent
b	Buoyancy
c	critical
CB	Cassie-Baxter
d	Drag
het	Heterogeneous
L	Lift
LV	Liquid–Vapor
M	Metal
O	Oxide
PL	Particle-Liquid
SL	Solid–Liquid
SV	Solid-Vapor
v	Molar volume
w	Wenzel
y	Young

Author details

María-Guadalupe González Solórzano[1], Rodolfo Morales-Dávila[1*],
Jafeth Rodríguez Ávila[2], Carlos Rodrigo Muñiz-Valdés[2] and Alfonso Nájera Bastida[3]

1 Instituto Politécnico Nacional-ESIQIE, Department of Metallurgy, Mexico

2 Facultad de Ingeniería, Universidad Autónoma de Coahuila, Blvd. Fundadores Km 13, Ciudad Universitaria, 25350, Arteaga Coahuila, México

3 Instituto Politécnico Nacional-UPIIZ, Metallurgical Engineering, Blvd. del Bote 202, Cerro del Gato, 98160, Zacatecas, México

*Address all correspondence to: rmorales@ipn.mx

IntechOpen

References

[1] Long M., Zuo X., Zhang L., Chen D., Kinetic modeling on nozzle clogging during steel billet continuous casting. ISIJ Int. 2010;50:712–720. DOI: 10.2355/isijinternational.50.712.

[2] Ni P., Jonsson L.T.I., Ersson M., Jönson PG., The use of an enhanced Eulerian deposition model to investigate nozzle clogging during continuous casting of steel. Metall. Mater. Trans. 2014;45:2414–2424. DOI: 10.1007/s11663-014-0145-5.

[3] Gutiérrez E., Garcia-Hernández S., Barreto J.deJ., Mathematical modeling of inclusions deposition at the upper tundish nozzle and the submerged entry nozzle. Steel Res. Int. 2016;87:1406–1416. DOI: 10.1002/srin.201500422.

[4] Gutiérrez E., Garcia-Hernández S., Barreto J.deJ., Mathematical analysis of the dynamic effects on the deposition of alumina inclusions inside the upper tundish nozzle. ISIJ Int. 2016;56:1394–1403. DOI: 10.2355/isijinternational.ISIJINT-2016-076.

[5] Barati H., Wu M., Holzmann T., Kharicha A., Ludwig A., Simulation of non-metallic inclusion deposition and clogging of nozzle. Miner. Met. Mater. Ser. 2018:149–158. DOI: 10.1007/978-3-319-72059-3_15.

[6] Snow R.B., Shea J.A., Mechanism of erosion of nozzles in open-hearth ladles. J. Am. Ceram Soc. 1949;32:187–194. DOI: 10.1111/j.1151-2916.1949.tb19766.x.

[7] Braun T.B., Elliott J.F., Flemings M. C., The clustering of alumina inclusions. Metall. Mater. Trans. 1979;10:171–184. DOI: 10.1007/BF02652461.

[8] Miki Y., Kitaoka H., Sakuraya T., Fujii T., Mechanism for separating inclusions from molten steel stirred with a rotating electro-magnetic field. ISIJ Int. 1992;32:142–149. DOI: 10.2355/isijinternational.32.142.

[9] Zhang L., Thomas B.G., State of the art in the control of inclusions during steel ingot casting. Metall. Mater. Trans. B 2006;37:733–761. DOI: 10.1007/s11663-006-0057-0.

[10] Sasai K., Mizukami Y., Mechanism of alumina adhesion to continuous caster nozzle with reoxidation of molten steel. ISIJ Int. 2001;41:1331–1339. DOI: 10.2355/isijinternational.41.1331.

[11] Tehovnik F., Burja J., Arh B., Knap M., Submerged entry nozzle clogging during continuous casting of Al-killed steel. 2015. Available from: https://hrcak.srce.hr/128965 (Accessed: 2020-09-18).

[12] Fukuda Y., Ueshima Y., Mizoguchi S., Mechanism of alumina deposition on alumina graphite immersion nozzle in continuous caster. ISIJ Int. 1992;32:164–168. DOI: 10.2355/isijinternational.32.164.

[13] Sasai K., Mizukami Y., Yamamura H., Reaction mechanism between alumina graphite immersion nozzle and low carbon steel. J. Iron Steel Inst. Jpn. 1993;79:1067–1074. DOI: 10.2355/tetsutohagane1955.79.9_1067.

[14] Sasai K., Mizukami Y., Reaction mechanism between alumina graphite immersion nozzle and low carbon steel. ISIJ Int. 1994;34:802–809. DOI: 10.2355/isijinternational.34.802.

[15] Singh S.N., Mechanism of alumina buildup in tundish nozzles during continuous casting of aluminum-killed steels. Metall. Mater. Trans. 1974;5:2165–2178. DOI: 10.1007/BF02643930.

[16] Kojola N., Ekerot S., Andersson M., Jönsson P.G., Pilot plant study of nozzle clogging mechanisms during casting of

REM treated stainless steels. Ironmak. Steelmak. 2011;38:1–11. DOI: 10.1179/030192310X12690127076398.

[17] Yokota S., Souma S.T., Guchi M., Asak Y., Hara S., Prevention of air suction from the contact-part between sliding gate and immersion nozzle. ISIJ Int. 1998;38:1346–1352. DOI: 10.2355/isijinternational.38.1346.

[18] Rackers K., Thomas B.G., Clogging in continuous casting nozzles. In: 78th Steelmaking Conf. Iron Steel Soc. April 2–5 1995; Nashville USA. p. 723–734.

[19] Savolainen J., Rousu A., Fabritius T., Mattila O, Sulasalmi P., Modelling of pressure distribution inside the SEN in a stopper-rod controlled system. Steel Res. Int. 2010;81:980–986. DOI: 10.1002/srin.201000012.

[20] Vermeulen Y., Coletti B., Blanpain B., Wollants P., Vleugels J., Material evaluation to prevent nozzle clogging during continuous casting of Al killed steels. ISIJ Int. 2002;42:1234–1240. DOI: 10.2355/isijinternational.42.1234.

[21] Barati H., Wu M., Kharicha A., Ludwig A., A transient model for nozzle clogging. Powder Techn. 2018;319:181–198. DOI: 10.1016/j.powtec.2018.01.053.

[22] Barati H., Wu M., Kharicha A., Ludwig A., Calculation accuracy and efficiency of a transient model for submerged entry nozzle clogging. Metall. Mater. Trans. B 2019;50:1428–1443. DOI: 10.1007/s11663-019-01551-x.

[23] Lee J.H., Kang Y.B., Growth of initial clog deposits during continuous casting of Ti-ULC steel formation and reduction of the initial deposits at nozzle/steel interface. ISIJ Int. 2020;60:426–435. DOI: 10.2355/isijinternational.ISIJINT-2019-384.

[24] Lee J.H., Kang M.H., Kim S.K., Kang Y.B., Oxidation of Ti added ULC steel by CO gas simulating interfacial

reaction between the steel and SEN during continuous casting. ISIJ Int. 2018;58:1257–1266. DOI: 10.2355/isijinternational.ISIJINT-2018-164.

[25] Lee J.H., Kang M.H., Kim S.K,. Kim J., Kim M.S., Kang Y.B., Influence of Al/Ti ratio in Ti-ULC steel and refractory components of submerged entry nozzle on formation of clogging deposits. ISIJ Int. 2019;59:749–758. DOI: 10.2355/isijinternational.ISIJINT-2018-672.

[26] Suito H., Ohta H., Characteristics of particle size distribution in early stage of deoxidation, ISIJ Int. 2006;46:33–41. DOI: 10.2355/isijinternational.46.33.

[27] Kubaschewski O., Alcock C.B., Metallurgical Thermochemistry, Pergamon Press. New York. 1979, 1.

[28] Tromp R.M., Hannon J.B., Thermodynamics of nucleation and growth, Surf. Rev. and Letters, 2002;9; 1565–1593.

[29] Li G., Suito H., Electrochemical measurement of critical supersaturation in Fe-O-M (M=Al, Si, and Zr) and Fe-O-Al-M (M=C, Mn, Cr, Si, and Ti) melts by solid electrolyte galvanic cell. ISIJ Int. 1997;37:762–769. DOI3: 10.2355/isijinternational.37.762.

[30] Van Ende Marie-Aline., Formation and morphology of non-metallic inclusions in aluminium killed steels [thesis]. Saint-Louis: Universite Catholique de Louvain, 2010.

[31] Wakoh M., Sano N., Behavior of alumina inclusions just after reoxidation, ISIJ Int. 2003;47;627–632.

[32] Porter D.A., Easterling KE, Sherif MY. Phase Transformations in Metals and Alloys, Chapman and Hall, 3er ed. London-Tokyo; 2009. 315 p. DOI: 10.1201/9781439883570.

[33] De Cooman B.C., Speer J.G., Fundamentals of Steel Product Physical

Metallurgy. 1st ed. Assn of Iron & Steel Engineers. 2011. 40 p.

[34] Kojima Y., Inouye M., Yamada Y., Solubility and diffusion of nitrogen in liquid iron-nickel and iron-cobalt alloys at 1600° C., Transactions ISIJ 1975;15: 599–605.

[35] Steinmetz E., Lindenberg H.U., Morphology of inclusions at aluminium deoxidation. Archiv Eisenhuttenwesen 1976;47:199–204.

[36] Adaba Menyelum-Obinn. Oxide Inclusion Evolution and Factors that Influence their Size and Morphology [thesis]. Missouri University of Science and Thechnology, 2019.

[37] Lindborg U., Torssell K., A collision model for the growth and separation of deoxidation products. Trans. Met. Soc. AIME, 1968; 242:94–102.

[38] Saffman P.G., Turner J.S., On the collision of drops in turbulent clouds. J. F!uid Mech. 1956;1:16–30.

[39] Miki Y., Kitaoka H., Sakuraya T., Fujii T., Mechanism for separating inclusions from molten steel stirred with a rotating electro-magnetic field. ISIJ Int. 1992;32:142–149. DOI: 10.2355/ isijinternational.32.142.

[40] Dekkers R., Jokanovic N., Rombout A., Blanpain B., Wollants P., Steel cleanliness during secondary metallurgy of high-grade quality electric steels. Steel. Res. Int. 2005;76:475–480. DOI: 10.1002/srin.200506042.

[41] Delgado M., SIMEC Operations, private communication, Steelmaking Manager, SIMEC Group, Special Steels Plant. Tlaxcala, Mexico, 2019.

[42] Zheng L., Malfliet A., Wollants P., Blanpain B., Guo M., Effect of alumina morphology on the clustering of alumina inclusions in molten iron. ISIJ Int. 2016;56:926–935. DOI: 10.2355/ isijinternational.ISIJINT-2015-561.

[43] Ooi H., Sekine M., Kasai G., On the Mechanisms of alumina cluster formation in molten iron. Tetsu-to-Hanage 1973;59:1078–1088. DOI: 10.2355/tetsutohagane1955.59.8_1078.

[44] Kingery W.D., Bowen H.K., Uhlmann D.R., Introduction to Ceramics. 2nd ed. Wiley; 1976. 474–475 p.

[45] Kuczynski G.C., Selft-diffusion in sintering of metallic particles. Trans. Met. Soc. AIME 1949;185:169–178. DOI: 10.1007/978-94-009-0741-6_33.

[46] González-Solórzano M.G., Morales R.D., Gutiérrez E., Guarneros J., Chattopadhyay K., Analysis of fluid flow of liquid steel through clogged nozzles: thermodynamics analysis and flow simulation. Steel. Res. Int. 2020;91. DOI: 10.1002/srin.202000049.

[47] Eustathopoulos N., Nicholas M.G., Devrit B., Wettability at High Temperatures. 1st ed. Pergamon Press: Amsterdam; 1999. 1 p.

[48] Suito H., Ohta H., Characteristics of particle size distribution in early stage of deoxidation. ISIJ Int. 2006;46:33–41. DOI: 10.2355/isijinternational.46.33.

[49] Rashidi M., Hestroni G., Barnejee S., Particle-turbulence interaction in a boundary layer. Int. Journal of Multiph. Flow 1990;16:935–949. DOI: 10.1016/ 0301-9322(90)90099-5.

[50] Simons S.J.R., Seville J.P.K., Adams M.J., Analysis of the rupture energy of pendular liquid bridges. Chem. Eng. Sci. 1994;49:2331–2339. DOI: 10.1016/0009-2509(94)E0050-Z.

[51] Diéguez-Salgado U., Investigation of particle attraction by steel/refractory and steel/gas interfaces and the associated relevance for clogging in casting processes [thesis]. Leoben; University, Austria, 2018.

[52] Liming Shi L., Bayless D., Comparison of boundary conditions for

predicting the collection efficiency of cyclones Pow. Tech. 2007;173:29–37. DOI: 10.1016/j.powtec.2006.11.022.

[53] Johnson K.L., Kendall K., Roberts A. D., Suface energy and the contact of elastic solids. In: Proceedings of the Royal Society A. 08 September 1971. p. 301–313. DOI: 10.1098/rspa.1971.0141.